

Chemical Strain Engineering of MAPbI₃ Perovskite Films

Yenal Yalcinkaya, Ilka M. Hermes, Tobias Seewald, Katrin Amann-Winkel, Lothar Veith, Lukas Schmidt-Mende, and Stefan A.L. Weber*

This study introduces a new chemical method for controlling the strain in methylammonium lead iodide (MAPbI₃) perovskite crystals by varying the ratio of Pb(Ac)₂ and PbCl₂ in the precursor solution. To observe the effect on crystal strain, a combination of piezoresponse force microscopy (PFM) and X-ray diffraction (XRD) is used. The PFM images show an increase in the average size of ferroelastic twin domains upon increasing the PbCl₂ content, indicating an increase in crystal strain. The XRD spectra support this observation with strong crystal twinning features that appear in the spectra. This behavior is caused by a strain gradient during the crystallization due to different evaporation rates of methylammonium acetate and methylammonium chloride as revealed by time-of-flight secondary ion mass spectroscopy and grazing incidence X-ray diffraction measurements. Additional time-resolved photoluminescence shows an increased carrier lifetime in the MAPbI₃ films prepared with higher PbCl₂ content, suggesting a decreased trap density in films with larger twin domain structures. The results demonstrate the potential of chemical strain engineering as a simple method for controlling strain-related effects in lead halide perovskites.

1. Introduction

Hybrid lead halide perovskites^[1–6] show remarkable properties such as a direct adjustable bandgap,^[7–9] high defect tolerance,^[10] and long charge carrier lifetimes^[11–13] that make them ideally suited as absorber materials for photovoltaic applications. An interesting effect that has been observed in many hybrid lead halide perovskite materials is that the optoelectronic properties can be strongly influenced by external or internal strain. Thus, strain engineering can be a useful method to control and tune the optoelectronic properties or structural stability of perovskite materials.^[14,15] For example, Zhu et al. showed improved charge extraction at the perovskite-hole transport layer interface by eliminating the strain gradient and thereby flattening the valence band.^[16] Kim et al. used strain engineering to relax the crystal lattice of formamidinium lead iodide (FAPbI₃), enabling improved solar

cell performance.^[17] In addition, strain engineering had also been used by various groups to increase the stability of perovskite structures. Zhao et al. demonstrated that strain engineering of MAPbI₃ by mechanically bending the substrate increased the stability.^[18] Strain engineering was also used to stabilize metastable phases such as CsPbI₃ and FAPbI₃ by the introduction of biaxial strain via cooling a perovskite crystal clamped to a ceramic substrate^[19] or applying strain by heteroepitaxially growing the perovskite on another perovskite material.^[20]

Another important strain-related effect observed in methylammonium lead iodide (MAPbI₃) crystals is the formation of sub-granular ferroelastic twin domains. Ferroelastic twin domains in tetragonal MAPbI₃ were first observed via piezoresponse force microscopy (PFM) by our group,^[21] followed by many others.^[22–25] The domains form due to the strain resulting from the cubic to tetragonal phase change at 57 °C. Strelcov et al. observed via polarized optical microscopy (POM) that mechanical stress leads to a rearrangement of the twin domains in MAPbI₃, supporting the conclusion that the domains are ferroelastic.^[26] Since our first report in 2016, ferroelastic twins have been observed by many other techniques, including transmission electron microscopy (TEM),^[24] X-ray diffraction (XRD),^[27] and neutron scattering.^[28]

The existence of a sub-granular domain structure raises the question whether these domains have an influence on the electronic transport properties. Recently, Xiao et al.^[29] concluded

Y. Yalcinkaya, K. Amann-Winkel, L. Veith, S. A. L. Weber
Max Planck Institute for Polymer Research
Ackermannweg 10, 55128 Mainz, Germany

E-mail: webers@mpip-mainz.mpg.de
Y. Yalcinkaya, K. Amann-Winkel, S. A. L. Weber
Institute of Physics
Johannes Gutenberg University Mainz
Duesbergweg 10-14, 55128 Mainz, Germany

I. M. Hermes
Leibniz Institute for Polymer Research Dresden e.V.
Institute of Physical Chemistry and Polymer Physics
Department Polymer Interfaces
Hohe Str. 6, 01069 Dresden, Germany

T. Seewald, L. Schmidt-Mende
Department of Physics
University of Konstanz
Universitätsstr. 10, 78464 Konstanz, Germany

 The ORCID identification number(s) for the author(s) of this article can be found under <https://doi.org/10.1002/aenm.202202442>.

© 2022 The Authors. Advanced Energy Materials published by Wiley-VCH GmbH. This is an open access article under the terms of the Creative Commons Attribution-NonCommercial License, which permits use, distribution and reproduction in any medium, provided the original work is properly cited and is not used for commercial purposes.

DOI: [10.1002/aenm.202202442](https://doi.org/10.1002/aenm.202202442)

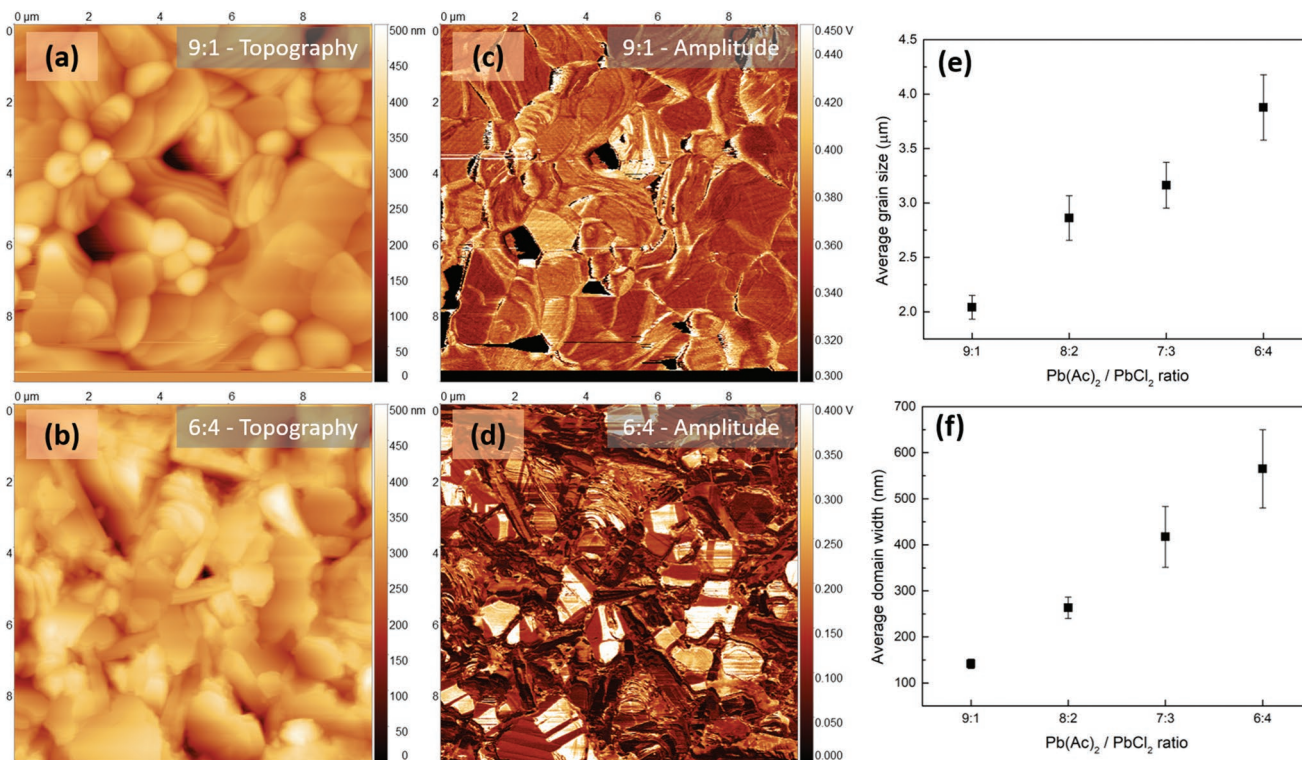


Figure 1. Topography and PFM amplitude images of MAPbI₃ thin films with Pb(Ac)₂/PbCl₂ ratios of a,c) 9:1, and b,d) 6:4. e) Average grain size and f) domain width profiles of MAPbI₃ thin films with different Pb(Ac)₂/PbCl₂ ratios.

from PL and lifetime mapping experiments that the ferroelastic twin domains are benign to recombination kinetics. To separate potential grain boundary effects, our group recently investigated large isolated MAPbI₃ grains. Using time-resolved PL microscopy, we found an anisotropic charge transport that was correlated to the ferroelastic twin domain structure in the crystal.^[30] In particular, the charge diffusion perpendicular to the ferroelastic domains was slower compared to the charge diffusion parallel to the domains.

Such an anisotropic diffusion would be interesting for guiding charge carriers, e.g., to the electrodes of an optoelectronic device. Thus, a targeted manipulation or engineering of the twin domain structure would be desirable. Next to domain manipulation through mechanical straining,^[26] we showed that the ferroelastic twin domain structure changes when using different cooling rates after annealing.^[30,31] Here, a slower cooling rate resulted in a more dense and ordered domain structure whereas a higher cooling rate lead to disordered and less dense twin domains. Lastly, Röhm et al. demonstrated the domain manipulation via a lateral electric field.^[32] However, all the domain manipulation methods mentioned above are not easy to scale up for mass production.

In this study, we introduce a new method for controlling the mechanical strain during the crystal growth via the composition of the precursor solution. In particular, we use different ratios of Pb(Ac)₂ and PbCl₂ to synthesize MAPbI₃ thin films on glass substrates in order to adjust the overall crystallization of MAPbI₃ films. Acetate and chloride anions were chosen because they require similar annealing temperatures for evaporation/sublimation while iodide-based synthesis requires higher annealing temperatures.^[33] Using a combination of PFM and XRD, we

observed an increase in crystal strain connected to an increase in the average twin domain size upon increasing the PbCl₂ content. Additionally, we observed a change from stripe-like to rectangular domains, an effect that has been connected to increased crystal strain.^[26] Based on time-of-flight secondary ion mass spectroscopy (ToF-SIMS) experiments, where we found an accumulation of chloride at the substrate interface, we suggest that the strain during crystal growth is caused by the combined effect of low temperature crystallization and ion exchange during annealing. This chloride accumulation is most likely caused by different evaporation rate of the methylammonium acetate (MA(Ac)) and sublimation rate of methylammonium chloride (MACl). Additional time-resolved photoluminescence (TRPL) showed an increased carrier lifetime in the MAPbI₃ films prepared with higher PbCl₂ content, suggesting a decreased trap density in films with larger twin domain structures.

2. Results and Discussion

2.1. Piezoresponse Force Microscopy (PFM)

We prepared several batches of MAPbI₃ films on glass with precursor ratios between 9:1 and 6:4 and investigated the topography and the lateral piezoresponse using AFM/PFM (Figure 1a-d; Figure S2, Supporting Information; details on the working mechanism of PFM are given in the Experimental Section). Figure 1e shows the average grain sizes obtained from several areas of the films with changing Pb(Ac)₂/PbCl₂ ratios. The most obvious effect of the the precursor ratio change is an increase in average grain size ($\langle d \rangle$) from $2.04 \pm 0.11 \mu\text{m}$ for the 9:1 Pb(Ac)₂/PbCl₂

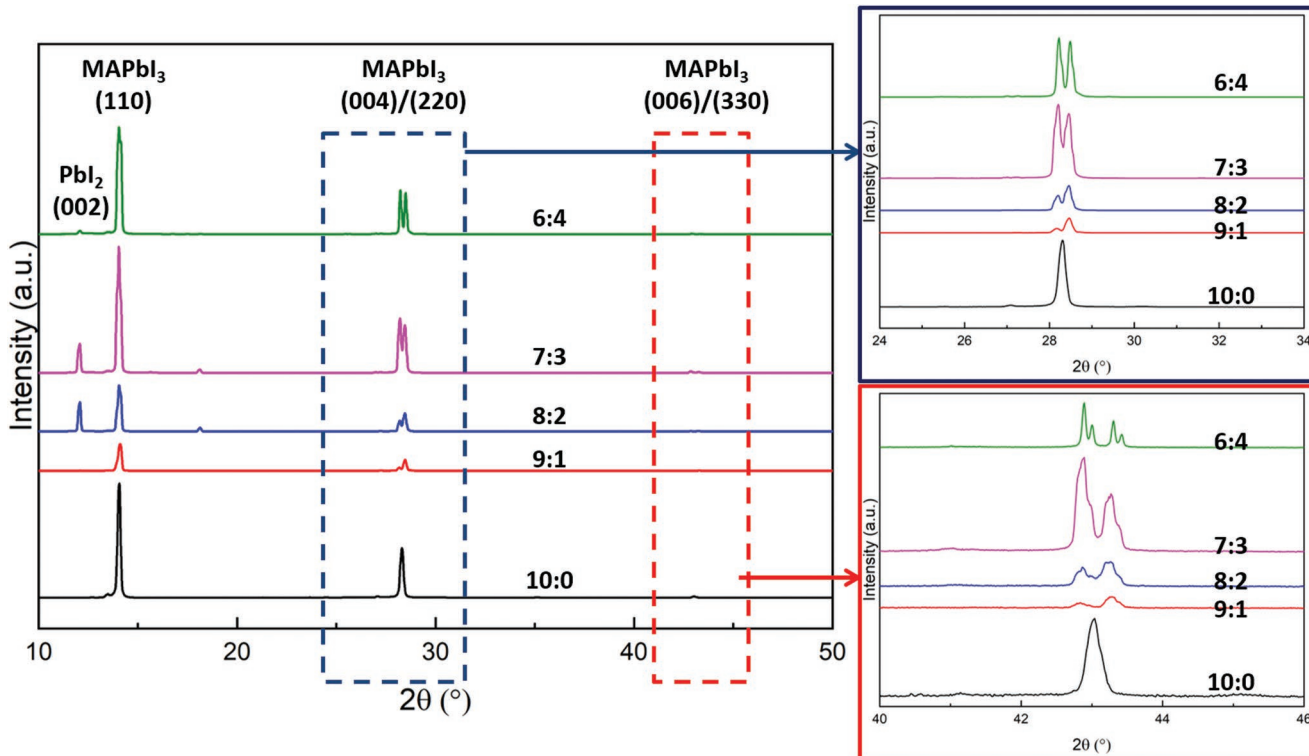


Figure 2. XRD patterns of MAPbI_3 thin films with $\text{Pb}(\text{Ac})_2/\text{PbCl}_2$ ratios of 10:0, 9:1, 8:2, 7:3, and 6:4. Intensities were shifted for clarity, the data are not normalized.

ratio to $3.9 \pm 0.3 \mu\text{m}$ for the 6:4 $\text{Pb}(\text{Ac})_2/\text{PbCl}_2$ ratio (Figure 1e). A MAPbI_3 film prepared from pure $\text{Pb}(\text{Ac})_2$ precursor had an even smaller average grain size of $0.85 \pm 0.31 \mu\text{m}$ (Figure S1, Supporting Information). The decrease in grain size upon lowering the PbCl_2 content comes from the decreased Cl or MACl content which speeds up the crystallization of perovskite and leads to smaller grains.^[33] Furthermore, the combined effect of MACl and DMF annealing seems to be causing a significant increase in grain size compared to MAPbI_3 film prepared from pure $\text{Pb}(\text{Ac})_2$ precursor. In addition to the grain size, the general grain morphology also changed upon decreasing $\text{Pb}(\text{Ac})_2/\text{PbCl}_2$ ratio. In between the perovskite grains we observed more pinholes and undefined structures (Figure 1b). On average, the density of pinholes and undefined structures increases with decreasing $\text{Pb}(\text{Ac})_2/\text{PbCl}_2$ ratio (Figure S2, Supporting Information), suggesting these structures could be caused by residual PbI_2 or MAPbCl_3 that forms after the spin coating.^[27] The reason for this effect could again be a slower crystallization in the MAPbI_3 film due to the lower volatility of MACl compared to $\text{MA}(\text{Ac})$. Later on, we will show that this interpretation is also supported by XRD (Figure 2), ToF-SIMS (Figure 3), and UV-Vis absorption (Figure S12, Supporting Information) results.

The lateral PFM amplitude images show the familiar striped ferroelastic domain structure^[21] (Figure 1c,d). Compared to MAPbI_3 films with 9:1 $\text{Pb}(\text{Ac})_2/\text{PbCl}_2$ ratio (Figure 1c), films prepared from the 6:4 precursor ratio show a less dense domain structure (Figure 1d). In particular, we observed an increase in the width of the ferroelastic twin domains with increasing PbCl_2 content. Figure 1f shows average ferroelastic twin domain width values gathered from various areas of the samples. The distances between the high amplitude and low amplitude areas

revealed an average domain width ($\langle w \rangle$) of $137 \pm 10 \text{ nm}$ for the MAPbI_3 film with 9:1 and $560 \pm 90 \text{ nm}$ and 6:4 $\text{Pb}(\text{Ac})_2/\text{PbCl}_2$ ratio, respectively (Figure 1f).

As twin domains are purely strain related, it seems obvious from the changing domain pattern that the strain in the films is influenced by different $\text{Pb}(\text{Ac})_2/\text{PbCl}_2$ ratios. The work by Strelcov et al.^[26] has demonstrated that external stress can alter the domain structure. Their results show that upon increasing the strain within the MAPbI_3 films the stripe-shaped domains evolve into larger areas. Furthermore, the emergence of non-90° domain angles were observed upon increased external stress.^[26] We also observed such domain shapes (Figure 1), suggesting that the precursor mixing with $\text{Pb}(\text{Ac})_2/\text{PbCl}_2$ or $\text{MA}(\text{Ac})$ and MACl increases the strain within the $\text{Pb}(\text{Ac})_2/\text{PbCl}_2$ structure.

2.2. X-Ray Diffraction

To support the hypothesis of precursor-induced strain adjustment in our MAPbI_3 films with different $\text{Pb}(\text{Ac})_2/\text{PbCl}_2$ ratios, we performed XRD measurements. In the XRD, all mixed precursor samples showed the typical reflections for MAPbI_3 with addition of PbI_2 (Figure 2; Figure S3, Supporting Information) and some unidentified weak peaks around 18° that may belong to intermediates or a Lewis acid-base adduct due to retarded crystallization caused by increased PbCl_2 .^[34] As the PbCl_2 amount increases, the intensity ratio of MAPbI_3 (110)/ PbI_2 (002) peaks also increases and reaches to a maximum value for 6:4 $\text{Pb}(\text{Ac})_2/\text{PbCl}_2$ ratio, resulting in quenched PbI_2 (002) signal in Figure 2. We also observed a peak splitting around 28° due to $\{00l\}/\{hk0\}$ twinning in MAPbI_3 films^[27] (Figure 2, blue box) in MAPbI_3

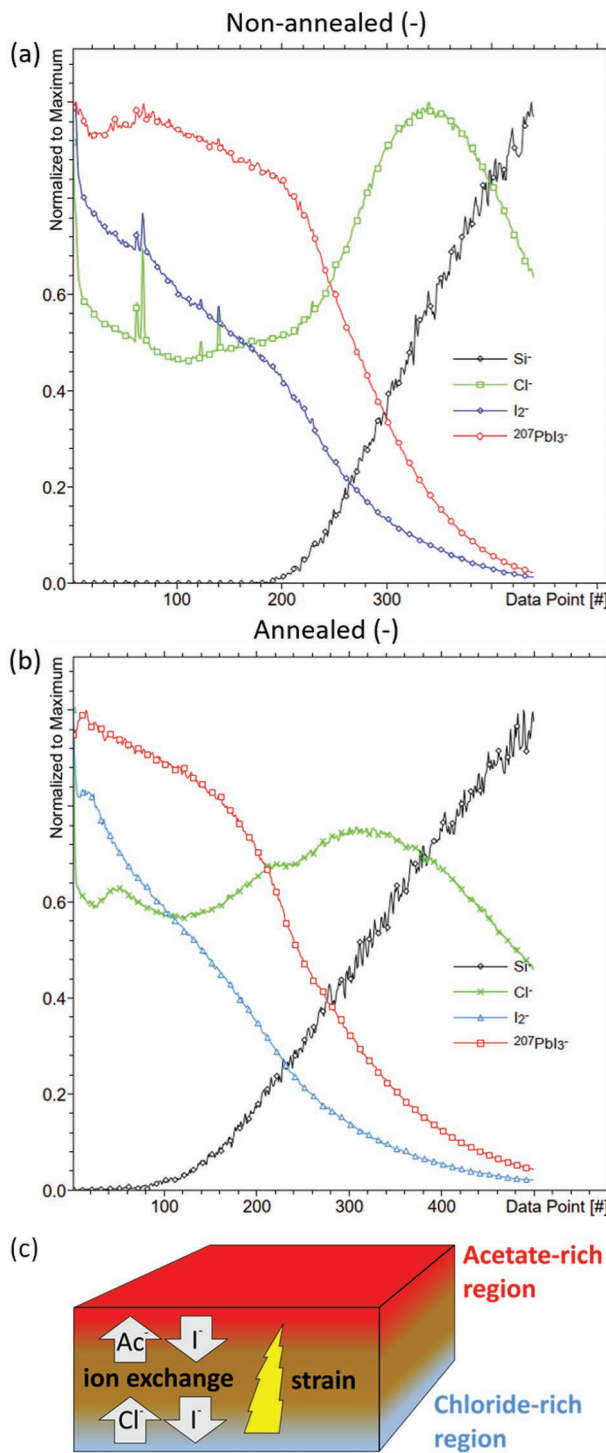


Figure 3. Chemical depth profiles of a) non-annealed and b) annealed MAPbI₃ film made with 6:4 Pb(Ac)₂/PbCl₂ ratio and c) illustration of strain mechanism.

films with Pb(Ac)₂/PbCl₂. The intensity ratio of the (004) peaks to the (220) peaks $\approx 28^\circ$ increased when the Pb(Ac)₂/PbCl₂ ratio was decreased. The lower inset of Figure 2 (red box) shows the XRD signal in the range between 40° and 46° . Again, as the Pb(Ac)₂/PbCl₂ ratio was decreased, the (006)/(330) peak inten-

sity ratios increased. Interestingly, we found a further splitting of the split peaks in samples prepared from a 6:4 Pb(Ac)₂/PbCl₂ ratio, resulting in four peaks $\approx 43^\circ$. Based on the work by Dang et al.,^[35] these additional peaks may belong to the (134) and (402) planes. Such further peak splitting in the XRD could be related to lower symmetry for smaller Pb(Ac)₂/PbCl₂ ratios as a result from the formation of non-90° domains. A similar observation in XRD pattern of MAPbI₃ was observed by Leonhard et al.^[36] where the emerging peaks disappeared upon further annealing, indicating strain relaxation. These results suggest that the larger domain areas in the PFM images in Figure 1b belong to {001} facets and that their XRD intensity increases due to increased area. Furthermore, the observation of a second peak splitting may indicate an increased residual strain resulted by different Pb(Ac)₂/PbCl₂.

To learn more about the overall strain behavior within the MAPbI₃ films, we analyzed the XRD peak shifts as a function of Pb(Ac)₂/PbCl₂ ratio. The position for MAPbI₃ (110) peak for 10:0, 9:1, 8:2, 7:3, and 6:4 Pb(Ac)₂/PbCl₂ ratios were observed at $\approx 14^\circ$. One important observation in MAPbI₃ (110) plane for 6:4 Pb(Ac)₂/PbCl₂ ratio is the emerging shoulder at 14.14° (Figure 2). This splitting of the (110) plane suggests that another twinning starts to take place in these samples, likely caused by a higher strain. The peak splitting trends of (004)/(220) and (006)/(330) suggest that the peak at the higher scattering angles belongs to {hk0} planes while the peak at the lower scattering angles belongs to the {00l} planes, possibly (002). Furthermore, the positions of split MAPbI₃ (004)/(220) peaks were observed at 28.32° (only (220)), $28.18/28.47^\circ$, $28.2/28.46^\circ$, $28.21/28.45^\circ$, and $28.23/28.49^\circ$ for 10:0, 9:1, 8:2, 7:3, and 6:4 Pb(Ac)₂/PbCl₂ ratios, respectively. It is safe to assume that strain controls the trends observed in the XRD measurements since the enlarged domains were also observed in PFM as a result of increased strain. Here, a shift to lower scattering angles in MAPbI₃ (110) plane for Pb(Ac)₂/PbCl₂ ratios lower than 9:1 that may indicate the emergence of another peak from the (002) plane. Alternatively, this shift may indicate lattice expansion based on Bragg's law and interplanar distance formulas (Equations S1 and S2, Supporting Information). Moreover, a shift to the higher scattering angles for MAPbI₃ (004) plane and a shift to lower scattering angles for MAPbI₃ (220) was observed with decreasing Pb(Ac)₂/PbCl₂ ratio that may indicate lattice shrinking and lattice expansion, respectively (Equations S1 and S2, Supporting Information).

Lastly, we have also performed an XRD measurement on a MAPbI₃ film made from a precursor solution containing only MAI and Pb(Ac)₂. This sample in particular was not annealed but only dried at room temperature in the glovebox since MA(Ac) is much more volatile compared to MACl and MAPbI₃ can form without any heat treatment. The resulting films had a very small grain structure, which made PFM experiments impossible. Therefore, the twinning was only monitored via XRD for this sample (Figure S4a, Supporting Information). The resulting XRD pattern exhibited larger peak splitting, even more distinct than MAPbI₃ with 6:4 Pb(Ac)₂/PbCl₂ ratio. This result supports the notion of room temperature twinning in MAPbI₃.^[28] Also, the stronger (004) signal in non-annealed MAPbI₃ film made from only MAI and Pb(Ac)₂ compared to annealed samples in Figure 2 is because of strain relaxation upon annealing.

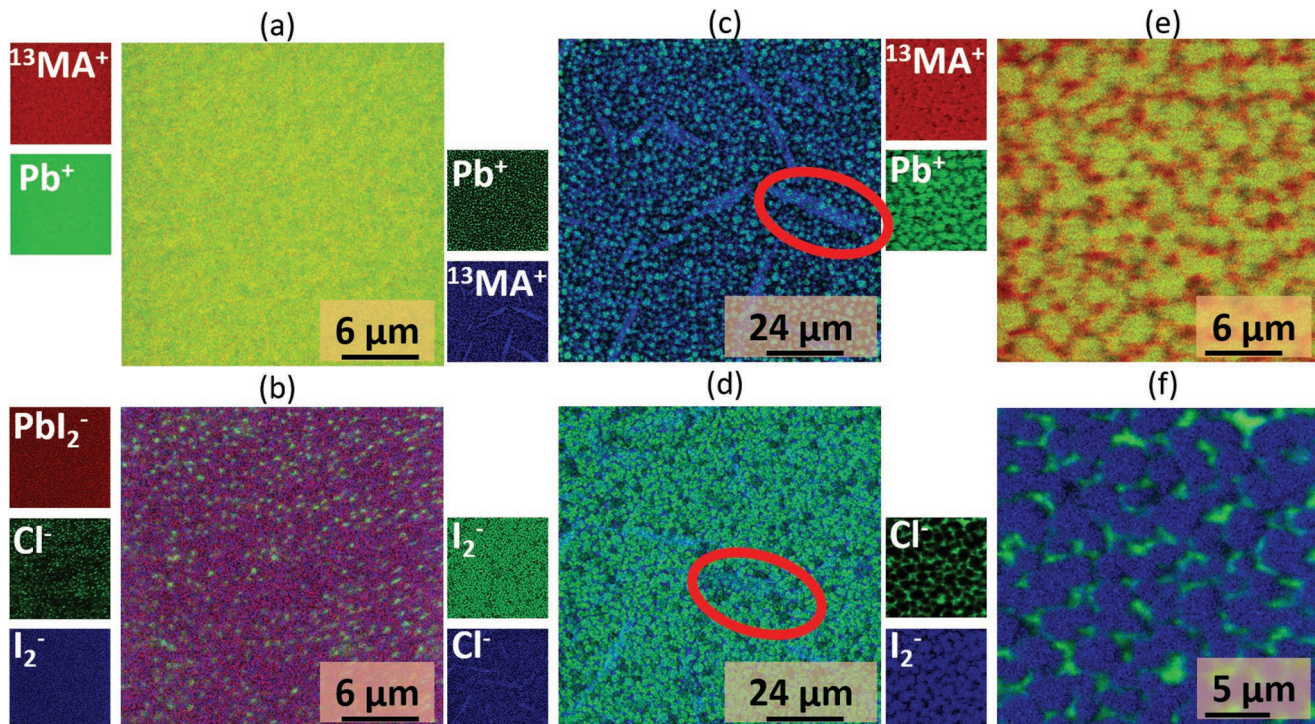


Figure 4. Lateral ion distributions in a,b) non-annealed and c,d,e,f) annealed MAPbI_3 films made from 6:4 $\text{Pb}(\text{Ac})_2/\text{PbCl}_2$ ratio.

2.3. Chemical Gradients and Strain Mechanism

To synthesize the MAPbI_3 , methylammonium iodide (MAI), lead acetate ($\text{Pb}(\text{Ac})_2$), and lead chloride (PbCl_2) precursors were utilized. In this synthesis, the molar ratio of MA precursor to Pb precursor is 3:1 as can given in Equation (1):



where X can be Ac, Cl, or I. The MAX compound is volatile and evaporates during the annealing of the film. The volatility and thus the evaporation rate of MAX depends on the X anion used in the precursor solution. Therefore, the crystallization kinetics in the MAPbI_3 film is controlled by the evaporation rate of the MAX compound.

The observed changes in the ferroelastic twin domain structure in PFM and the peak splitting behavior in the XRD spectra suggest a correlation between the strain in the MAPbI_3 films and the $\text{Pb}(\text{Ac})_2/\text{PbCl}_2$ ratio in the precursor solution. A recent study by Medjahed et al.^[27] has investigated the strain in MAPbI_3 films prepared from a 3MAI/PbCl₂ solution by monitoring the twinning via XRD. According to this study, MAPbCl_3 forms within the film prior to annealing and I⁻/Cl⁻ ion exchange occurs during annealing. This process gives rise to strain formation within the MAPbI_3 film and eventually results in twin formation.

To investigate chemical kinetics within the perovskite film, we carried out ToF-SIMS. The profiles for both PbI_3^- and Cl⁻ show a pronounced chemical gradient within the film (Figure 3a,b). In the non-annealed film, we observed elevated levels of Cl⁻ at the bottom of the film compared to static/cen-

tral part of the profile line. As suggested previously, there might be volatile compounds on the surface involving Cl⁻ that could be the reason for high Cl⁻ concentration on the surface. The high Cl⁻ concentration in the depths of the film on the other hand shows that Cl⁻ ions tend to localize closer to the substrate in the mixed precursor MAPbI_3 film. A similar behaviour has been reported for pure MAI/PbCl₂ films.^[37] A similar trend was also observed for Cl⁻ in the annealed MAPbI_3 film, as well, however with an increased uniformity through the film. This can be an indication of I⁻/Cl⁻ ion exchange that leads to the formation of MAPbI_3 .

The depth profiles in both pristine and annealed MAPbI_3 films show I⁻ and PbI_3^- signals with the opposite trend of Cl⁻. After the precursor deposition, MAPbI_3 grains form closer to the surface while Cl-rich species stay at the bottom of the film. Upon annealing, MACl reaches the surface through the ion exchange. This ion exchange reaction of MAPbCl_3 is expected give rise to a vertical strain gradient. An illustration of this vertical ion exchange reaction is given in Figure 3c.

The depth profiles for positive ions (Figure S7, Supporting Information) show a uniform Pb⁺ ion distribution and a slight gradient in MA⁺ ion distribution. The non-uniform distribution of MA⁺ ion could also be contributing to the vertical strain gradient as observed before.^[38]

To investigate a potential strain gradient along the vertical direction of the film, we employed grazing incidence X-ray diffraction (GIXRD). GIXRD enables to change the X-ray penetration into the film by changing the incidence angle, providing depth-dependent crystal structure information. The GIXRD spectra of a MAPbI_3 film with 6:4 $\text{Pb}(\text{Ac})_2/\text{PbCl}_2$ ratio shows a change in XRD reflection around 14° (Figure S6a,

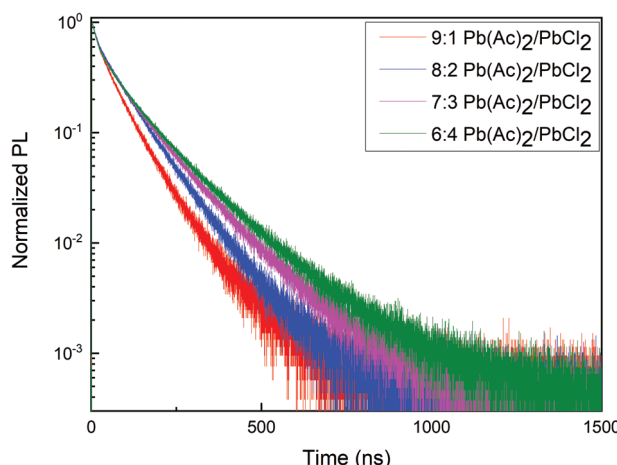


Figure 5. PL lifetimes of MAPbI_3 thin films with $\text{Pb}(\text{Ac})_2/\text{PbCl}_2$ ratios of 9:1, 8:2, 7:3, and 6:4.

Supporting Information). Deconvolution of the signal reveals a clear shift in the lattice parameters as the X-ray penetration into the perovskite film changes (Figure S6b, Supporting Information). These shifts are a clear signature of a vertical strain gradient.

The lateral chemical distribution was also determined using ToF-SIMS on non-annealed and annealed MAPbI_3 films with 6:4 $\text{Pb}(\text{Ac})_2/\text{PbCl}_2$ ratio (Figure 4). The ion distribution in the non-annealed MAPbI_3 film reveals uniform distribution of MA^+ , Pb^+ , and I_2^- ions after spin coating, whereas The Cl^- ions show a distribution pattern (Figure 4a,b). Based on the information we obtained from XRD measurements on non-annealed samples (Figure S5, Supporting Information), perovskite films at this stage should be consisting of MAPbI_3 and MAPbCl_3 . Therefore, we suggest the Cl -rich areas in the film are mostly MAPbCl_3 areas where the acetate-rich areas quickly transform into MAPbI_3 . Upon annealing, some morphological and chemical changes occurred within the perovskite film: MA^+ and Cl^- needle-like structures are prominent in the ToF-SIMS images (blue images in Figure 4c,d, marked with red), similar to the needle structures that we observed in the AFM images (Figure 1b). In contrast, the Pb^+ distribution was much more homogeneous (Figure 4c), whereas the I_2^- concentration was reduced in the needle-like structures (Figure 4d), suggesting these structures could be MACl that forms after I^-/Cl^- ion exchange. At larger magnification (Figure 4e,f), we see that grain interiors are rich in MA^+ , Pb^+ , and I_2^- , whereas the exterior of the grains is rich in Cl^- . However, there are small areas where the MA^+ and Pb^+ maps do not exactly match. These map mismatches suggest that the structures outside of MAPbI_3 grains could belong to structures such as PbI_2 and MACl that is not sublimated yet. In addition, we observed small amounts of Cl^- inside of the MAPbI_3 grains, suggesting a minor Cl^- doping could be taking place during fabrication. The ion maps show that next to a vertical chemical gradient there is also a lateral chemical gradient within the perovskite films (Figures 3 and 4). Since the correlation between the vertical chemical gradient and the strain gradient in the perovskite film is well established through our GIXRD results (Figure S6a,b, Supporting Information) and

supported by other studies,^[27,38] we conclude that lateral strain will be present within the films, as well.

2.4. Optical Measurements

Ferroelastic domain walls distort the local crystalline order and might form energetic barriers.^[30,39] In our earlier study, we found an alternating polarization at the domain walls that could act as shallow traps states or scattering centres, affecting the charge carrier dynamics.^[30] To study the effect of different domain morphologies on charge carrier lifetimes, we conducted TRPL measurements on our MAPbI_3 films with different $\text{Pb}(\text{Ac})_2/\text{PbCl}_2$ ratios (Figure 5). We fitted the results bi-exponentially to obtain lifetime parameters. We found that the carrier lifetime increased from 68.47 ± 0.23 ns for the film with 9:1 ratio to 104.35 ± 0.24 ns for the 6:4 $\text{Pb}(\text{Ac})_2/\text{PbCl}_2$ ratio (all values are given in Table S1, Supporting Information). This trend suggests the charged carriers move more freely in case of lower $\text{Pb}(\text{Ac})_2/\text{PbCl}_2$ ratios where the density of ferroelastic domain walls is decreased since the low energy barriers caused by the domain walls are eliminated. This result is in an agreement with our previous findings and the previously proposed energetic barriers theory. Furthermore Zhang et al. discovered that the charge carrier mobility in MAPbI_3 is plane dependent, i.e., anisotropic,^[40] offering an explanation for the energy barriers caused by ferroelastic twin domains.

To monitor the presence of additional phases and the optical properties, we performed UV-vis spectroscopy on the MAPbI_3 films with all the different $\text{Pb}(\text{Ac})_2/\text{PbCl}_2$ ratios (Figure S12, Supporting Information) where all samples showed an absorption band edge ≈ 780 nm. The absorption edge ≈ 600 nm that is visible in all spectra comes from PbI_2 which is in an agreement with the PbI_2 signal that we observed in XRD measurements. Furthermore, a new peak at 390 nm emerged belonging to MAPbCl_3 at any $\text{Pb}(\text{Ac})_2/\text{PbCl}_2$ ratio below 8:2. This matches with the expectation since MAPbCl_3 forms when PbCl_2 is used or increased in the precursor solution,^[27] which was also supported by ToF-SIMS results (Figure 3) and non-annealed XRD results (Figure S5, Supporting Information). Furthermore, the absorption decreased with decreasing $\text{Pb}(\text{Ac})_2/\text{PbCl}_2$ ratio due to decreasing amount of MAPbI_3 in the obtained film. This is possibly a result of the slow crystallization of MAPbI_3 due to the presence of PbCl_2 . Nevertheless, the MAPbCl_3 phase could not be detected by the XRD measurements in Figure 2, most likely due to the low MAPbCl_3 content in the films. In addition, we calculated Tauc plots (Figure S13, Supporting Information) from the absorption data from UV-vis results (Figure S12, Supporting Information). The bandgap of MAPbI_3 films slightly decreased with decreasing $\text{Pb}(\text{Ac})_2/\text{PbCl}_2$ ratio (Figures S13 and S14, Supporting Information). Since the bandgap of MAPbI_3 is the same for (110) and (001) planes,^[40] the bandgap change can be attributed to increased strain as suggested elsewhere.^[16]

3. Conclusion

In this work, we have shown a chemical route to control the strain in MAPbI_3 thin films by using different $\text{Pb}(\text{Ac})_2/\text{PbCl}_2$

ratios in the precursor solution. Using PFM and XRD, we monitored the internal structure; in particular, the formation of ferroelastic twin domains—a signature of internal strain. The PFM results showed an increase in the average ferroelastic twin domain areas as the $\text{Pb}(\text{Ac})_2/\text{PbCl}_2$ ratio decreased. The XRD results confirmed that this increase was accompanied by an increase in lattice strain. We suggest that this strain increase is caused by the volatility difference of $\text{MA}(\text{Ac})$ and MACl that eventually leads to crystallization rate differences in various regions in the film. This difference leads to room temperature formation of highly strained MAPbI_3 in $\text{MA}(\text{Ac})$ areas and I^-/Cl^- exchange occurs in Cl -rich areas resulting in increased strain with increased PbCl_2 amount. The chemical gradient and the resulting strain gradient were observed via ToF-SIMS and XRD measurements, respectively. To observe the effect of the resulting ferroelastic twin domain configurations on the charge carrier dynamics, we conducted TRPL measurements. The presence of larger ferroelastic domains implies a reduction in the overall domain wall density, which leads to longer charge carrier lifetimes.^[30]

Our work shows that the crystal strain and thereby the formation of ferroelastic twin domains can be chemically manipulated by simply changing the ratio of different precursors without the need to apply any external force. This strategy offers a simple and scalable route to achieve a favorable domain arrangement in MAPbI_3 -based devices, enabling faster and more efficient charge extraction. Even beyond domain engineering in MAPbI_3 , chemical strain engineering is a promising idea for strain engineering in many other other lead halide perovskite materials.

4. Experimental Section

Materials: Methylalmonium iodide (MAI) was purchased from Greatcell Energy. Lead acetate ($\text{Pb}(\text{Ac})_2$) for perovskite precursor, 98.0% purity) and lead chloride (PbCl_2 , 99.999%) were purchased from Tokyo Chemical Industry and Sigma-Aldrich, respectively. Anhydrous dimethylformamide (DMF) was purchased from Sigma Aldrich.

Perovskite Film Preparation: Glass substrates were brushed with Hellmanex on both sides and washed with hot tap water and milliQ water followed by drying with an air gun. The cleaned substrates were subjected to UV-Ozone treatment (FHR UVOH 150 LAB, 250 W) for 30 min with oxygen feeding rate of 1 L min^{-1} right before spin coating.

Two precursor solutions were prepared for the film preparation. Precursor solution 1 was prepared with MAI (477.0 mg, 3 mol), $\text{Pb}(\text{Ac})_2$ (325.3 mg, 1 mol), and DMF (1 mL) while precursor solution 2 was prepared with MAI (238.5 mg, 1.5 mol), PbCl_2 (137.0 mg, 0.5 mol), and DMF (500 μL). The precursor solutions 1 and 2 were mixed in 9:1, 8:2, 7:3, and 6:4 volume ratios before the fabrication. The perovskite film fabrication was carried out by static spin coating, which was performed at 4000 rpm (1000 rpm s^{-1}) for 1 min after smearing 100 μL solution over the substrate. After the spin coating, all the samples were dried at room temperature for 10 min. After drying, all samples were annealed in DMF vapor atmosphere at 100°C for 10 min. Glass petri dishes were used to obtain the DMF vapor atmosphere. The DMF vapor media were prepared before the coating started. The films were first put on the hotplate outside of the petri dish until they turned black (≈ 3 seconds) then put under DMF vapor atmosphere. Number of samples per petri dish were changed from 1 to 4. However, the amount of DMF should be changed accordingly. 15 μL DMF per film was used for the annealing process. All processes were carried out in a nitrogen glovebox.

Piezoresponse Force Microscopy Measurements: Piezoresponse force microscopy (PFM) is an Atomic force microscopy (AFM) mode, which is

used to detect electromechanical material properties on the nanometer scale. A conductive tip is used to detect the response of the sample to an AC voltage.

Lateral piezoresponse force microscopy (PFM) measurements were performed on an Asylum Research MFP-3D AFM from Oxford Instruments together with a Zürich Instruments HF2 lock-in amplifier in an argon filled glovebox (O_2 and $\text{H}_2\text{O} < 1\text{ ppm}$). The measurements were carried out with platinum-iridium coated SCM PIT-V2 cantilevers from Bruker with a nominal resonance frequency of 70 kHz and a spring constant of $\approx 2.5 \text{ nN nm}^{-1}$. The measurement of the PFM signal was performed at an AC excitation voltage with a peak amplitude of 2 V at the lateral contact resonance at $\approx 700 \text{ kHz}$ to take advantage of the resonance enhancement.

X-ray Diffraction Measurements: X-ray diffraction (XRD) patterns were taken with Rigaku SmartLab using $\text{Cu K}\alpha$ radiation. Diffractograms had been recorded in “0”–“0” geometry, using a Göbel mirror and automatic sample alignment. The scanning rate was 2° min^{-1} in steps of 0.01° . The total beam exposure time was 30 min.

Time of Flight Secondary Ion Mass Spectroscopy: ToF-SIMS experiments were performed using a TOF.SIMS5 (NCS) instrument (IONTOF GmbH, Münster, Germany) with 30 keV Bi³⁺ primary ions and 5 keV Ar1500 cluster ions for sputtering at a 45° angle. Surface imaging was facilitated using the ultimate imaging mode at a current of 0.05 pA at a cycle time of 100 μs . Dual beam depth profiling was conducted on an analysis area of $200 \times 200 \mu\text{m}^2$ with a sputter area of $500 \times 500 \mu\text{m}^2$ at a sputter current of 2.5 nA.

Optical Measurements: Absorption data was collected using a Cary5000 UV-vis-NIR spectrometer by Agilent equipped with an integrating sphere. Time-resolved photoluminescence was conducted via time-correlated single photon counting on a FluoTime300 spectrometer by PicoQuant at an emission wavelength of 770 nm, following pulsed 485 nm excitation at a repetition rate of 500 kHz.

Supporting Information

Supporting Information is available from the Wiley Online Library or from the author.

Acknowledgements

Y.Y., S.A.L.W., T.S., and L.S.-M. acknowledge the SPP2196 project (Deutsche Forschungsgemeinschaft) for funding. K.A.-W. acknowledges support from the Carl-Zeiss-Stiftung.

Open access funding enabled and organized by Projekt DEAL.

Conflict of Interest

The authors declare no conflict of interest.

Data Availability Statement

The data that support the findings of this study are available from the corresponding author upon reasonable request.

Keywords

ferroelasticity, halide perovskites, strain engineering, twinning

Received: July 18, 2022

Revised: July 22, 2022

Published online:

- [1] A. Kojima, K. Teshima, Y. Shirai, T. Miyasaka, *J. Am. Chem. Soc.* **2009**, *131*, 6050.
- [2] M. M. Lee, J. Teuscher, T. Miyasaka, T. N. Murakami, H. J. Snaith, *Science* **2012**, *338*, 643.
- [3] H.-S. Kim, C.-R. Lee, J.-H. Im, K.-B. Lee, T. Moehl, A. Marchioro, S.-J. Moon, R. Humphry-Baker, J.-H. Yum, J. E. Moser, M. Grätzel, N.-G. Park, *Sci. Rep.* **2012**, *2*, 1.
- [4] J. J. Yoo, S. Wieghold, M. C. Sponseller, M. R. Chua, S. N. Bertram, N. T. P. Hartono, J. S. Tresback, E. C. Hansen, J.-P. Correa-Baena, V. Bulović, T. Buonassisi, S. S. Shin, M. G. Bawendi, *Energy Environ. Sci.* **2019**, *12*, 2192.
- [5] O. A. Jaramillo-Quintero, R. S. Sanchez, M. Rincon, I. Mora-Sero, *J. Phys. Chem. Lett.* **2015**, *6*, 1883.
- [6] A. Ashar, N. Ganesh, K. Narayan, *Adv. Electron. Mater.* **2018**, *4*, 1870012.
- [7] L. Protesescu, S. Yakunin, M. I. Bodnarchuk, F. Krieg, R. Caputo, C. H. Hendon, R. X. Yang, A. Walsh, M. V. Kovalenko, *Nano Lett.* **2015**, *15*, 3692.
- [8] C. C. Stoumpos, C. D. Malliakas, M. G. Kanatzidis, *Inorg. Chem.* **2013**, *52*, 9019.
- [9] T. J. Jacobsson, J.-P. Correa-Baena, M. Pazoki, M. Saliba, K. Schenk, M. Grätzel, A. Hagfeldt, *Energy Environ. Sci.* **2016**, *9*, 1706.
- [10] K. X. Steirer, P. Schulz, G. Teeter, V. Stevanovic, M. Yang, K. Zhu, J. J. Berry, *ACS Energy Lett.* **2016**, *1*, 360.
- [11] M. B. Johnston, L. M. Herz, *Acc. Chem. Res.* **2016**, *49*, 146.
- [12] S. D. Stranks, G. E. Eperon, G. Grancini, C. Menelaou, M. J. Alcocer, T. Leijtens, L. M. Herz, A. Petrozza, H. J. Snaith, *Science* **2013**, *342*, 341.
- [13] D. Shi, V. Adinolfi, R. Comin, M. Yuan, E. Alarousu, A. Buin, Y. Chen, S. Hoogland, A. Rothenberger, K. Katsiev, Y. Losovyj, X. Zhang, P. A. Dowben, O. F. Mohammed, E. H. Sargent, O. M. Bakr, *Science* **2015**, *347*, 519.
- [14] E. G. Moloney, V. Yeddu, M. I. Saidaminov, *ACS Mater. Lett.* **2020**, *2*, 1495.
- [15] H. Yuce, C. A. Perini, J. Hidalgo, A.-F. Castro-Méndez, C. Evans, P. F. Betancur, J. N. Vagott, Y. An, K. Bairley, M. M. Demir, J.-P. Correa-Baena, *Opt. Mater.* **2021**, *111806*.
- [16] C. Zhu, X. Niu, Y. Fu, N. Li, C. Hu, Y. Chen, X. He, G. Na, P. Liu, H. Zai, Y. Ge, Y. Lu, X. Ke, Y. Bai, S. Yang, P. Chen, Y. Li, M. Sui, L. Zhang, H. Zhou, Q. Chen, *Nat. Commun.* **2019**, *10*, 1.
- [17] G. Kim, H. Min, K. S. Lee, D. Y. Lee, S. M. Yoon, S. I. Seok, *Science* **2020**, *370*, 108.
- [18] J. Zhao, Y. Deng, H. Wei, X. Zheng, Z. Yu, Y. Shao, J. E. Shield, J. Huang, *Sci. Adv.* **2017**, *3*, eaao5616.
- [19] J. A. Steele, H. Jin, I. Dovgaliuk, R. F. Berger, T. Braeckeveldt, H. Yuan, C. Martin, E. Solano, K. Lejaeghere, S. M. Rogge, C. Notebaert, W. Vandecasteele, K. P. F. Janssen, B. Goderis, E. Debroye, Y.-K. Wang, Y. Dong, D. Ma, M. Saidaminov, H. Tan, Z. Lu, V. Dyadkin, D. Chernyshov, V. V. Speybroeck, E. H. Sargent, J. Hofkens, M. B. J. Roeffaers, *Science* **2019**, *365*, 679.
- [20] Y. Chen, Y. Lei, Y. Li, Y. Yu, J. Cai, M.-H. Chiu, R. Rao, Y. Gu, C. Wang, W. Choi, H. Hu, C. Wang, Y. Li, J. Song, J. Zhang, B. Qi, M. Lin, Z. Zhang, A. E. Islam, B. Maruyama, S. Dayeh, L.-J. Li, K. Yang, Y.-H. Lo, S. Xu, *Nature* **2020**, *577*, 209.
- [21] I. M. Hermes, S. A. Bretschneider, V. W. Bergmann, D. Li, A. Klasen, J. Mars, W. Tremel, F. Laquai, H.-J. Butt, M. Mezger, R. Berger, B. J. Rodriguez, S. A. L. Weber, *J. Phys. Chem. C* **2016**, *120*, 5724.
- [22] B. Huang, G. Kong, E. N. Esfahani, S. Chen, Q. Li, J. Yu, N. Xu, Y. Zhang, S. Xie, H. Wen, P. Gao, J. Zhao, J. Li, *npj Quantum Mater.* **2018**, *3*, 1.
- [23] H. Röhm, T. Leonhard, M. J. Hoffmann, A. Colsmann, *Energy Environ. Sci.* **2017**, *10*, 950.
- [24] M. U. Rothmann, W. Li, Y. Zhu, U. Bach, L. Spiccia, J. Etheridge, Y.-B. Cheng, *Nat. Commun.* **2017**, *8*, 1.
- [25] Y. Liu, L. Collins, R. Proksch, S. Kim, B. R. Watson, B. Doughty, T. R. Calhoun, M. Ahmadi, A. V. Levlev, S. Jesse, S. T. Retterer, A. Belianinov, K. Xiao Huang, B. G. Sumpter, S. V. Kalinin, B. Hu, O. S. Ovchinnikova, *Nat. Mater.* **2018**, *17*, 1013.
- [26] E. Strelcov, Q. Dong, T. Li, J. Chae, Y. Shao, Y. Deng, A. Gruverman, J. Huang, A. Centrone, *Sci. Adv.* **2017**, *3*, e1602165.
- [27] A. A. Medjahed, P. Dally, T. Zhou, N. Lemaitre, D. Djurado, P. Reiss, S. Pouget, *Chem. Mater.* **2020**, *32*, 3346.
- [28] J. Breternitz, M. Tovar, S. Schorr, *Sci. Rep.* **2020**, *10*, 1.
- [29] X. Xiao, W. Li, Y. Fang, Y. Liu, Y. Shao, S. Yang, J. Zhao, X. Dai, R. Zia, J. Huang, *Nat. Commun.* **2020**, *11*, 1.
- [30] I. M. Hermes, A. Best, L. Winkelmann, J. Mars, S. M. Vorpahl, M. Mezger, L. Collins, H.-J. Butt, D. S. Ginger, K. Koynov, S. A. L. Weber, *Energy Environ. Sci.* **2020**, *13*, 4168.
- [31] S. M. Vorpahl, R. Giridharagopal, G. E. Eperon, I. M. Hermes, S. A. Weber, D. S. Ginger, *ACS Appl. Energy Mater.* **2018**, *1*, 1534.
- [32] H. Röhm, T. Leonhard, M. J. Hoffmann, A. Colsmann, *Adv. Funct. Mater.* **2020**, *30*, 1908657.
- [33] W. Zhang, M. Saliba, D. T. Moore, S. K. Pathak, M. T. Hörantner, T. Stergiopoulos, S. D. Stranks, G. E. Eperon, J. A. Alexander-Webber, A. Abate, A. Sadhanala, S. Yao, Y. Chen, R. H. Friend, L. A. Estroff, U. Wiesner, H. J. Snaith, *Nat. Commun.* **2015**, *6*, 1.
- [34] D.-K. Lee, D.-N. Jeong, T. K. Ahn, N.-G. Park, *ACS Energy Lett.* **2019**, *4*, 2393.
- [35] Y. Dang, Y. Liu, Y. Sun, D. Yuan, X. Liu, W. Lu, G. Liu, H. Xia, X. Tao, *CrystEngComm* **2015**, *17*, 665.
- [36] T. Leonhard, H. Röhm, F. J. Altermann, M. J. Hoffmann, A. Colsmann, *J. Mater. Chem. A* **2021**, *9*, 21845.
- [37] E. L. Unger, A. R. Bowring, C. J. Tassone, V. L. Pool, A. Gold-Parker, R. Cheacharoen, K. H. Stone, E. T. Hoke, M. F. Toney, M. D. McGehee, *Chem. Mater.* **2014**, *26*, 7158.
- [38] Y. Liu, A. V. Levlev, L. Collins, A. Belianinov, J. K. Keum, M. Ahmadi, S. Jesse, S. T. Retterer, K. Xiao, J. Huang, B. G. Sumpter, S. V. Kalinin, B. Hu, O. S. Ovchinnikova, *Adv. Electron. Mater.* **2020**, *6*, 1901235.
- [39] M. Coll, A. Gomez, E. Mas-Marza, O. Almora, G. Garcia-Belmonte, M. Campoy-Quiles, J. Bisquert, *J. Phys. Chem. Lett.* **2015**, *6*, 1408.
- [40] J. Zhang, K. Wang, Q. Yao, Y. Yuan, J. Ding, W. Zhang, H. Sun, C. Shang, C. Li, T. Zhou, S. Pang, *ACS Appl. Mater. Interfaces* **2021**.